DOI: 10.37190/abb/208295

Multiscale vibration response analysis and fatigue damage prediction after idiopathic scoliosis kyphosis surgery

Yuxuan Zhang[1], Rongchang Fu[1*], Pengju Li[1]

[1]School of Mechanical Engineering, Xinjiang University, Urumqi, Xinjiang, China

*Corresponding author: Rongchang Fu, School of Mechanical Engineering, Xinjiang University, Urumqi, Xinjiang, China, e-mail address: rongchangfu2010@xju.edu.cn

Submitted: 4th June 2025

Accepted: 15th July 2025

Abstract

Purpose: The multiscale vibratory response of the spine following orthopedic surgery in patients with idiopathic scoliosis and postoperative traumatic fatigue injury remains largely unexplored.

Methods: This paper analyzes the postoperative macroscopic spine model in the modal, time, and frequency domains to obtain the vibration response of the patient's entire spine. Subsequently, the stresses in the cortical bone mesoscopic bone units around the surgically damaged interface were calculated using submodeling algorithms. The pore stresses and pore flow velocities of the osteocytes were then derived from the stresses of the mesoscopic bone units to predict fatigue damage at the fusion surface.

Results: The findings indicated that the first three orders of intrinsic frequency exerted the most significant influence on the spine model. The maximum stress of the bone unit was observed at the X3 bone plate on the left side of the fusion surface, and the maximum pore pressure and flow velocity of the bone cells occurred at the X4 on the right side of the fusion surface. The medical implants used in spinal orthopedics, titanium cages and pedicle nails, change the mobility of the adjacent segments and also create a stress shielding effect that impacts the fusion of bone tissues.

Conclusions: Microscopic bone cell synapses experience greater pore pressures and pore flow velocities in the vibration environment compared to those under the static environment, which may promote cell growth. Vibration at low loads typically does not induce fatigue damage to cancellous bone at the fusion surface of medical implants.

Key words: Modal, Frequency domain analysis, Time domain analysis, Submodels, Fatigue damage, Finite elements

1. Introduction

Idiopathic scoliosis (IS) is a prevalent three-dimensional structural deformity of the spine, characterized by anteroposterior convex deformity of the vertebral bodies, lateral curvature, and vertebral rotation [3]. If severe IS is not corrected through surgery in a timely manner, the degree of deformity will gradually deteriorate, resulting in postural abnormalities, thoracic compression, and even endangering life [3], [32]. Treatment options for severe IS typically include osteotomy, along with internal fixation with pedicle nails, or placement of a titanium cage for osseointegration if the intact vertebrae are amputated [28]. The vibration environment can adversely affect the spine [12], [14], and prolonged exposure to vibration may cause cyclic stretching and compression of the spine, leading to fatigue of the

surrounding muscles as well as damage to the soft tissues [17], which can particularly lead to cause degenerative disc disease [20]. Furthermore, the vibration environment can influence the patient's postoperative period. It may also affect the degree of postoperative interbody fusion and even causes damage to the vertebrae (such as loosening of the pedicle rod system and titanium cage fusion device, stress shielding effect, degradation of neighboring vertebrae, and fatigue damage to cancellous bone). Therefore, it is necessary to analyze the macroscopic vibratory response of the spine in the postoperative period.

Although macroscopic analysis is the cornerstone of biomechanical studies [6], it often hinders the understanding of growth and damage at the bone cell level. Finite element analysis of mesoscopic microstructures can effectively target human bone under disuse, physiological, overuse, and pathological overload [1], [7]. The macroscopic loading of bone exposed to vibration in the human body generates distinct mechanical signals in the meso- and micro-structures of bone, and these differences in the mechanical signals are also reflected at the macroscopic level [10]. By adopting a multiscale finite element approach to investigate the biomechanics of postoperative IS, we can explore the relationship between macroscopic loading and meso- and microstructures after IS, as well as further examine the mechanical effects of medical titanium alloy implant materials on the patient's bone structure. The mesoscopic level primarily pertains to the bone unit, while the microscopic level focuses mainly on the bone Lacunar-Canalicular System (LCS).

This paper takes idiopathic lateral kyphosis patients as an example. Given that vibration experiments on patients after orthopaedic surgery are unreasonable and can easily cause harm to patients, finite element methods are used in this paper to analyze the spine, bone units, and bone cells of the patients in a vibration environment at macroscopic, mesoscopic, and microscopic levels. Compared with previous studies on human vibration mechanics, the response of bone units and bone cells to the vibration environment is further investigated. Our findings provide new insights for physicians to formulate orthopaedic surgery programs, offer new ideas for further research on the mechanics of vibration damage to bone structures, and establish a theoretical basis for preventing patients from suffering from secondary injuries.

2. Materials and Methods

2.1. Ethics

The patient provided written informed consent for the use of their clinical data in this study.

2.2. Data sources

The subject of this study is a patient with idiopathic scoliosis. The patient is a female, 47

years old, with a height of 140 cm and a weight of 39 kg. In a standing state, the proximal Cobb angle of the upper thoracic vertebrae is 32 °, the Cobb angle of the thoracolumbar vertebrae is 67 °, and the Cobb angle of the lumbar vertebrae is 40 °. The patient has a particularly severe kyphosis, with a kyphosis Cobb angle of 124 °. The Cobb angle of the proximal thoracic vertebrae is 21 °, the Cobb angle of the thoracolumbar vertebrae is 32 °, the Cobb angle of the lumbar vertebrae is 27 °, and the kyphosis Cobb angle is 34°. The patient was from the Sixth Affiliated Hospital of Xinjiang Medical University and gave her consent for participation in this study, and the study was performed by all authors.

2.3. Finite element modeling

A 64-slice helical CT scan of the patient's thoracolumbar spine was conducted with slice spacings of 0.5918 mm and 0.7578 mm, and a total of 509 images in DICOM format were obtained. To construct the macroscopic model, the CT scan dataset was imported into Mimics 21.0 (Materialise, Belgium) for threshold setting and manual segmentation, and the 3D geometric model of the thoracolumbar spine was obtained. Subsequently, the 3D model in Mimics was exported in STL format to Geomagic Studio 12.0 (Geomagic, USA) for surface configuration and smoothing optimization. The Geomagic Studio model was imported into SolidWorks 2023 (Dassault Systèmes, USA) in IGS format to construct the intervertebral disc, nucleus pulposus, and articular cartilage. At last, the vertebral cortical bone, vertebral cancellous bone, and ligaments were imported into Hypermesh 2021 (Altair, USA), and all the components were meshed. Mesoscopic models were developed in Abaqus 2021 (Simulia, USA), while microscopic models were created in COMSOL Multiphysics 5.6 (Comsol AB, Sverige).

The finite element modeling process established in this paper is illustrated in Fig. 1. The model included various components, including vertebral cortical bone, vertebral cancellous bone, endplates, nucleus pulposus, annulus fibrosus, articular cartilage, and seven associated ligaments. The ligaments were composed of the supraspinous ligament (SSL), interspinous ligament (ISL), transverse ligament (ITL), ligamentum flavum (LF), capsule ligament (CL), posterior longitudinal ligament (PLL), and anterior longitudinal ligament (ALL). The vertebral cortical bone was simulated using triangular linear strain shell units with a thickness of 1 mm [15]; the cancellous bone was simulated using tetrahedral first-order linear solid units; the endplates were simulated using rectangular linear strain shell units; the annulus fibrosus matrix, medulla oblongata, commissures, and medical titanium staple rod system were simulated using eight-node hexahedral solid units; the ligaments were simulated using one-dimensional linear rod units as linear elastic isotropic material [36].

According to the orthopedic plan proposed by the physician based on this patient's actual condition, the required implants were modeled in SolidWorks 2023. The orthopedic procedure was simulated in accordance with the surgical plan, which is detailed as follows: after surgical exposure of the patient's spine, the T8 vertebral body was resected using a snatch forceps and a bone knife, along with the bilateral articular synchondrosis joints of L1. The corresponding widths of the vertebral plates and ligaments were also resected. A titanium cage was placed in the original T8 vertebrae, and 16 pedicle screws (universal Xinjunte) were implanted in the T6-L2 vertebrae under the guidance of a C-arm. The T6-T10 pedicle screws had a diameter of 4 mm, a nail length of 35 mm, a thread length of 20 mm, and a thread depth of 0.5 mm. The T11-T12 pedicle screws had a diameter of 5.5 mm, a nail length of 35 mm, a thread length of 20 mm, and a thread depth of 0.5 mm. The L1-L2 pedicle root nail has a diameter of 6 mm, a nail length of 40mm, a thread length of 25mm, and a thread depth of 0.5mm. Two connecting rods were installed at T7-T9 and L1-L2. The resected part of the vertebral body was utilized as bone graft material, and after implanting a large amount of autogenous bone graft fusion, the incision was closed layer by layer.

A bone unit is a component of bone at the mesoscopic scale, consisting of Havers canal and multilayered concentric bone plates, bone plate media, and bonding wires [31]. In this paper, bone units with six layers of concentric bone plates were established on the lower surface of T7 vertebra and the upper surface of T9 vertebra in the upper, lower, left, and right directions, numbered (X1-X4) and (S1-S4), respectively.

The LCS is the primary component of bone at the microscopic scale. In this paper, one LCS was selected from each of the aforementioned eight bone cells for microscopic study, maintaining the same numbering as the corresponding bone cell. The bone cells comprise a cell membrane, cytoplasm, and nucleus inside, with each part idealized as a homogeneous ellipsoidal sphere [29]. Considering the symmetry of the microscopic LCS model, the number of cellular synapses was set at 6, with traps and tubules enveloping the cell cytosol and synapses [30].

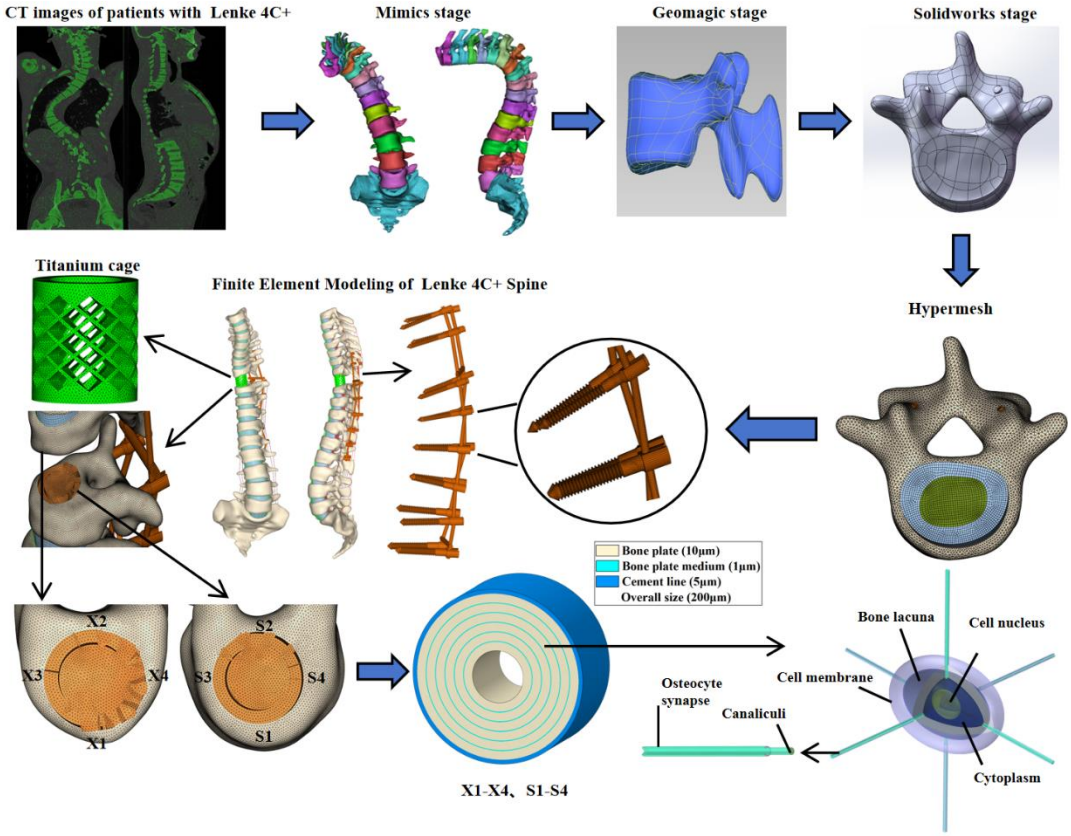

Fig. 1. The process of developing the finite element model of the spine.

2.4. Materials of the model

The material properties of the macroscopic spine components and bone units are presented in Table 1. The dimensions of each structure of the microscopic LCS finite element model are detailed in Table 2. The microscopic LCS is defined as isotropic materials, and the material properties of each structure of the finite element model are provided in Table 3.

170 **Table 1.** Characteristics of spinal components [16], [19], [38].

Spinal components	Elastic modulus/MPa	Poisson's ratio	Cross-sectional area/mm^2	Element type	Density/ (g·cm^{-3})
Cortical	12000	0.3		S3/S4R	1.7
Cancellous bone	100	0.2		C3D4/C3D5	1.1
Endplate	24.3	0.4		S4R	1.2
Nucleus pulposus	1.0	0.49		C3D8R	1.02
Fibrous rings	4.2	0.3		C3D8R	1.05
Articular capsule	20	0.3		C3D8R	1
ALL	7.8	0.3	63.7	T3D2	1
PLL	10	0.3	20	T3D2	1
LF	15	0.3	40	T3D2	1
ISL	10	0.3	40	T3D2	1
SSL	8	0.3	30	T3D2	1
ITL	10	0.3	1.8	T3D2	1
CL	20	0.3	30	T3D2	1
Titanium cage	110000	0.34		C3D4	4.4
Medical titanium alloy nail rod system	110000	0.34		C3D4	4.4
Bone plate	21500	0.3		C3D8R/C3D6	1
Bone plate medium	120	0.3		C3D6	1
Cement line	6850	0.49		C3D6	1

171 **Table 2.** Dimensions of each structure of the microscopic LCS finite element model [9], [30].

Components	Value/nm	Components	Value/nm
The side length of the bone matrix	40000	The short axis of the nucleus	4000
The height of the nucleus	2500	The long axis of the nucleus	5000
The long axis of the cytoplasm	14000	The short axis of the cytoplasm	8000
The height of the cytoplasm	8000	The thickness of the cell membrane	200
The diameter of the cell process	440	The thickness of lacunar	2100
The thickness of the canalicular	80		

Table 3. Material properties of each structure of the microscopic LCS finite element model [4], [9], [16], [19], [30], [38].

Property	Nucleus	Cytoplasm	Cell membrane	Cell process	lacuna	canaliculi	Bone matrix
Modulus elasticity /(Pa)	1000	250	4470	4470	16E+09	43000	2.0E+10
Poisson's ratio	0.3	0.49	0.3	0.3	0.38	0.3	0.3
Solid density /(kg/m^3)	2000	2000	800	800	1800	1200	2000
Dynamic viscosity/(Pa·s)	0.001	0.001	0.001	0.001	0.000697	0.000697	0.000697
Porosity	0.1	0.1	0.2	0.2	0.08	0.1	0.05
Permeability /(m^2)	1.0E-20	1.0E-18	1.0E-18	1.0E-18	1.0E-19	1.0E-18	1.0E-20
Biot-wills coefficient	2.5E-01	2.5E-01	2.5E-01	2.5E-01	1.4E-01	1.8E-01	1.32E-01
Compressibility /(1/Pa)	4.0E-10	4.0E-10	4.0E-10	4.0E-10	4.0E-10	4.0E-10	4.0E-10
Fluid density /(kg/m3)	1000	1000	1000	1000	1000	1000	1000

2.5. Boundary conditions

Modal analysis provides intrinsic frequencies and vibration modes. The mass of the upper body significantly affects the dynamic response of the human spine, and studies on the body mass distribution of Chinese people have pointed out [27] that the upper body accounts for approximately 52% of the total body weight, with the head, neck, and shoulders comprising about 22% of the body weight. Therefore, a simplified mass point of 10.5 kg was added to the upper surface of the first thoracic vertebrae, T1, in the macroscopic spine model [18], along with a simplified mass point of 0.45 kg added to each side of the T1-L5 vertebrae. All degrees of freedom of the lower surface of the sacrum were fixed [37]. The boundary conditions for frequency-domain analysis were as follows: a 40 N sinusoidal axial excitation was applied to the upper surface of the T1 vertebral body within a frequency range of 0-30 Hz [18], and an equivalent damping ratio of 0.08 was adopted [16]. For time-domain analysis, the boundary conditions were set as follows: a cyclic load of 40 N corresponding to the first three orders of intrinsic frequencies of the spine model was applied to the apical surface of the T1 vertebral body [17], and the spine was analyzed from 0 to 6 seconds postoperatively at a step

size of 0.01 seconds. The mesoscopic model of the bone cell utilized a submodeling function based on Saint-Venant's principle. The submodeling method is a finite unit technique designed to obtain more accurate solutions for specific regions of the model, with the displacement values calculated by the macroscopic model serving as the boundary conditions of the submodel. The boundary conditions were imposed on the exterior of the bonding line of the bone cell.

In the microscopic model of bone cells, the microstrain results of the mesoscopic model were applied to the Y-axis of the model in the form of displacement loads $S_1 = -a + a * \cos(2\pi ft)$ and $S_2 = a - a * \cos(2\pi ft)$ in negative-to-negative and negative-to-positive directions, respectively. Here, f denotes the loading frequency with a value of 1, and a is a quarter of the maximum displacement amplitude.The specific boundary conditions are shown in Fig. 2.

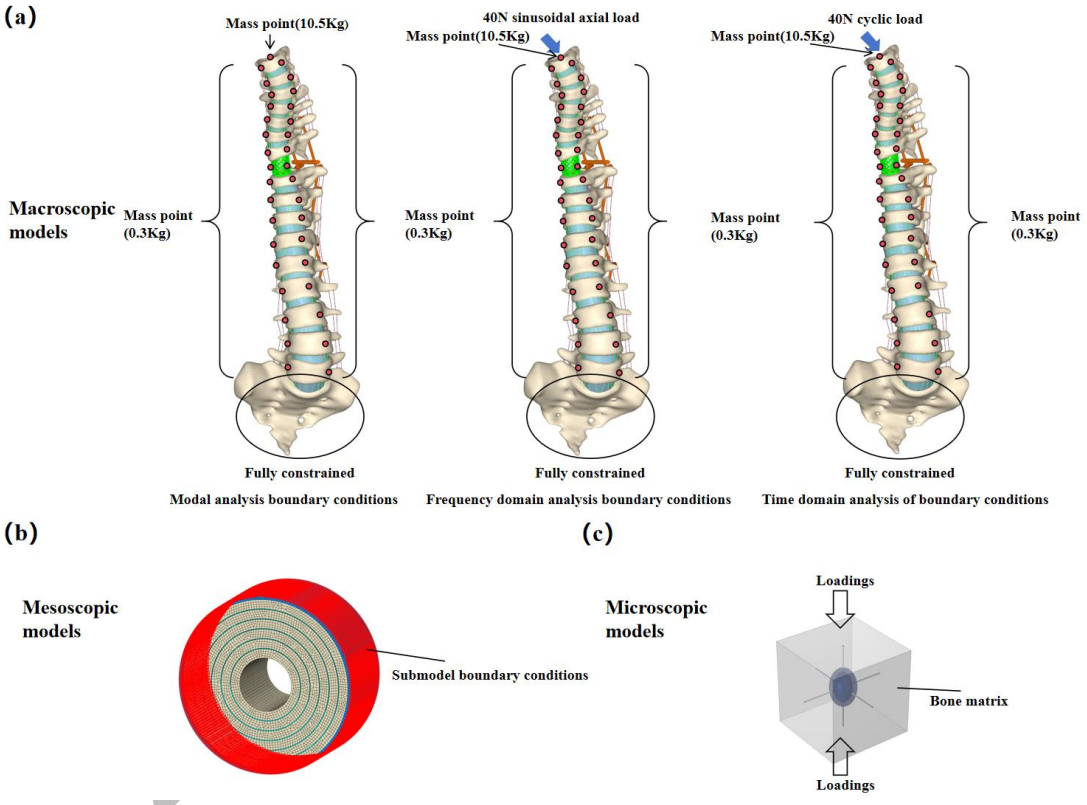

Fig. 2. Schematic representation of the boundary conditions of the finite element model (a-c).

2.6. Model validation

In this paper, the modular thoracolumbosacral spine (T1-S1) finite element model can be decomposed into several segments for validity verification. Firstly, the T11-L1 segment was selected, the lower end of L1 was fixed, and a moment of 10 Nm was applied to the upper end of T11 to simulate forward flexion, backward extension, lateral bending, and torsion

conditions. Additionally, a uniform pressure and tension of -200N, -100N, 100N, 200N, and 300N were applied, respectively. The simulation results were compared with the literature of the isolated experiments [24], as shown in Fig. 3 (a).

Similarly, the L4-L5 segment was selected, the lower end of L5 was fixed, and uniform axial loads of 500, 1000, 1500, and 2000 N were applied to the upper end of L4. Meanwhile, a moment of 10 Nm was applied to the upper end of L4 under the positive pressure of 500 N on L4 to simulate the forward flexion, backward extension, lateral bending, and torsion working conditions. The axial displacement and mobility of the vertebrae [2], [8], [21]–[23], [33], [34] are illustrated in Fig. 3(b), compared with the disembodied experiment. Under identical conditions, the finite element simulation results have the same trend and close values as the results of the ex vivo experiment, thereby confirming the reliability and validity of the model.

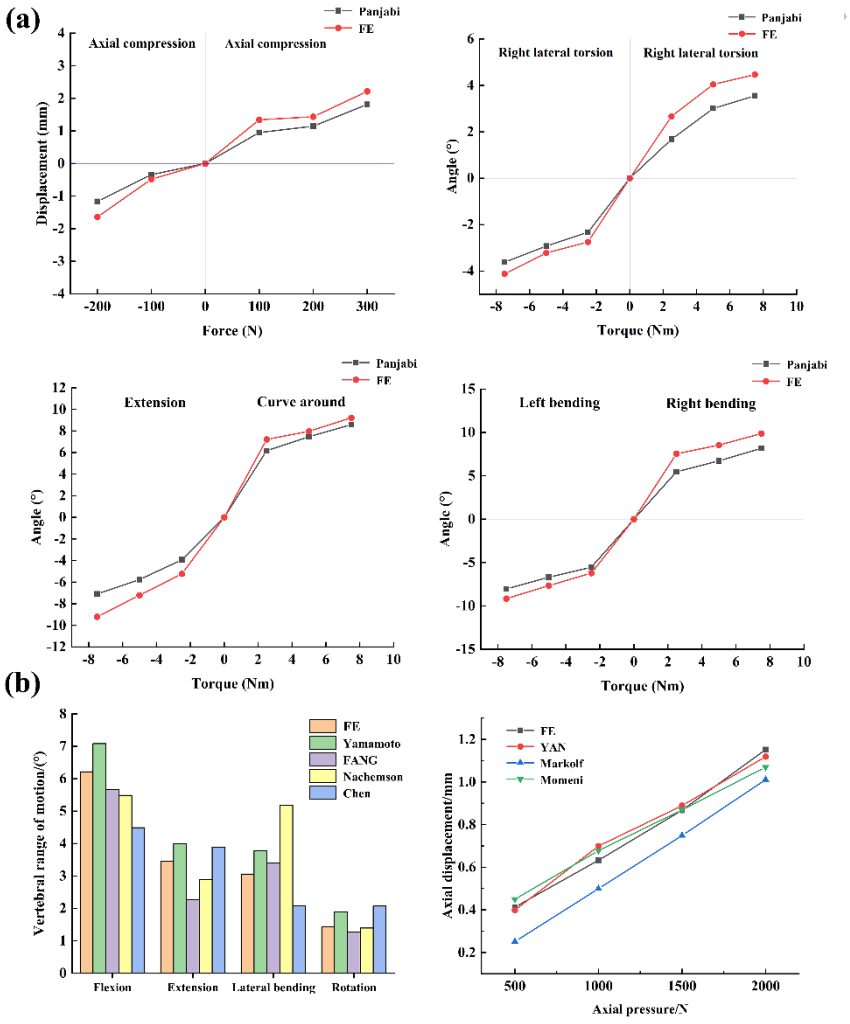

Fig. 3. Comparative validation plot of the validity of the finite element model for this study (a-b).

3. Results

3.1. Modal analysis results

The macroscopic spine model was subjected to modal analysis, and the first four orders of modes were selected for analysis. The results are as follows: the first-order mode was 0.59 Hz, with a vibration pattern characterized by the left-right swing of the thoracolumbar segment along the X-axis; the second-order mode was 0.85 Hz, with a vibration pattern characterized by anteroposterior and posterior flexion of the thoracolumbar segment along the Y-axis; the third-order mode was 5.29 Hz, with a vibration pattern characterized by up-down stretching of the thoracolumbar segment along the Z-axis. The fourth-order mode is 5.75 Hz, with a vibration pattern characterized by the torsion of the thoracolumbar segment along the Z-axis. Figure 4 illustrates the modal vibration pattern.

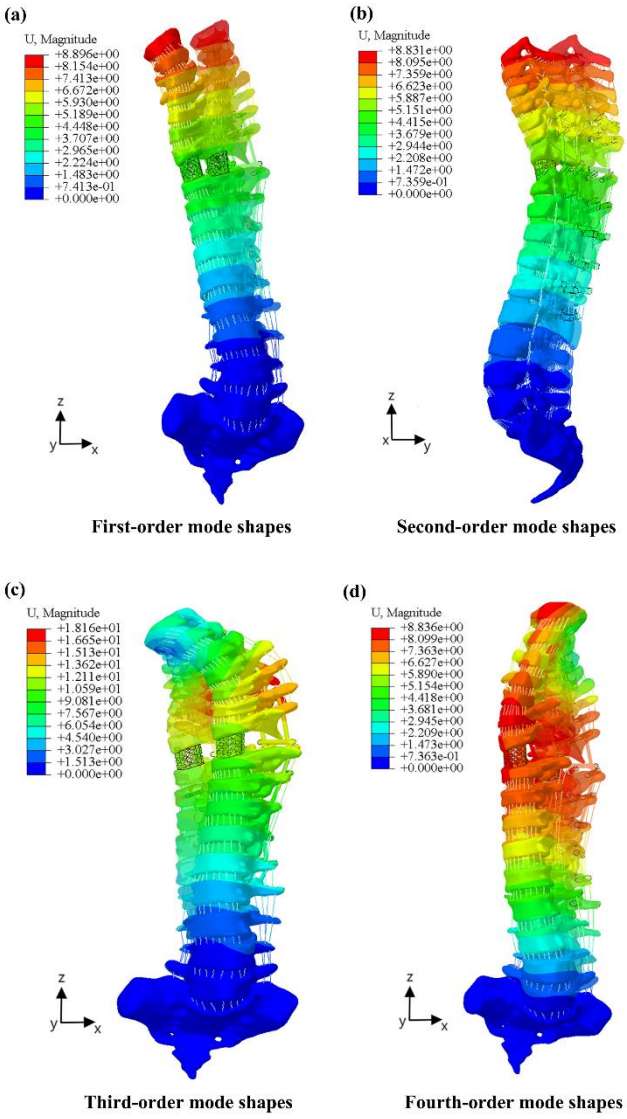

Fig. 4. Plot of the first four orders of modal vibrations (a-d).

3.2. Macro model frequency domain and time domain analysis results

The frequency domain and analysis results of the spine model are demonstrated in Fig. 5. The findings indicate that the primary resonance frequencies of the spine following the patient's orthopedic surgery correspond to the first three orders of the intrinsic frequency, with the most significant resonance near the first two orders of the intrinsic frequency. The first-order intrinsic frequency resonance of thoracic vertebrae T7 and T9-T10 reached it maximum in the X-direction of T7, with a value of -256.99 mm; the second-order intrinsic frequency resonance reached it maximum in the Y-direction of T7, with a value of 62.63 mm; the third-order intrinsic frequency resonance reached its maximum in the Y-direction of T7, with a value of 7.29 mm. The first-order intrinsic frequency resonance of lumbar vertebrae L1-L3 reached its maximum in the Y-direction of L3, with a value of -256.99 mm. The first order intrinsic frequency resonance of the lumbar vertebrae L1-L3 reached its maximum in the X direction of L3, with a value of -310.54 mm; the second-order intrinsic frequency resonance reached its maximum in the Y direction of L3, with a value of 74.87 mm; the third order intrinsic frequency resonance reached its maximum in the Y direction of L3, with a value of 7.35 mm.

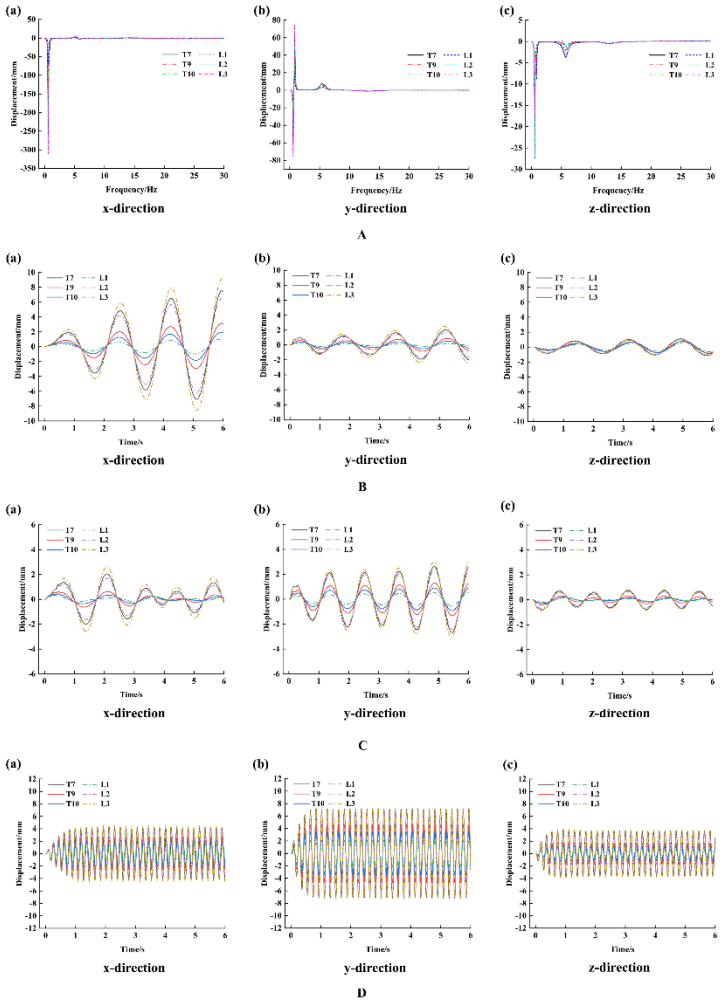

Fig. 5. Frequency domain analysis results of the thoracic as well as lumbar spine of the postoperative spine model (A), and time domain results of the first three orders of frequency excitation (B-D).

The time-domain results demonstrate that, under the external excitation at the first-order intrinsic frequency, the displacements of the thoracic vertebrae T7, T9-T10, and the lumbar vertebrae L1-L3 in the X-direction gradually increase, and the displacements in the Y-direction are smaller relative to those in the X-direction but larger than those in the Z-direction. Under the external excitation of the second-order intrinsic frequency, both thoracic and lumbar vertebrae exhibited a steady-state response, with minimal displacement response in the three directions. Similarly, under the external excitation at the third-order intrinsic frequency, the thoracic and lumbar vertebrae remained in steady-state response, and the displacements were also small. Among the first three orders of intrinsic frequency, the first-order intrinsic frequency excitation exerted the most substantial effect on the vibration displacement of the thoracic and lumbar spine. Therefore, the macroscopic model under the

excitation of the first-order intrinsic frequency was continued to be analyzed at both mesoscopic and microscopic levels.

The intervertebral discs are more susceptible to degenerative diseases than the vertebral body, so the annulus fibrosus and nucleus pulposus are analyzed for stress and strain. Meanwhile, the spinal column after surgery incorporates medical implants such as pedicle pins and titanium cages, which also require analysis regarding stress and strain. In this way, the stress shielding effect of medical implants under the whole-body vibration environment was further evaluated. The results of the time-domain mechanical property analysis are illustrated in Fig. 6. It can be seen that the annulus fibrosus and the nucleus pulposus have the highest stress under the third-order intrinsic frequency excitation, with a maximum annulus fibrosus pressure of 1.28 MPa at T3/T4 and a maximum nucleus pulposus pressure of 0.51 MPa at T9/T10. The implant, the pedicle nail, and the titanium cage have the highest stress under the third-order intrinsic frequency excitation, with a maximum stress of 84.32 MPa in the pedicle nail at T7 and 95.32 MPa in the titanium cage at T9/T10, respectively.

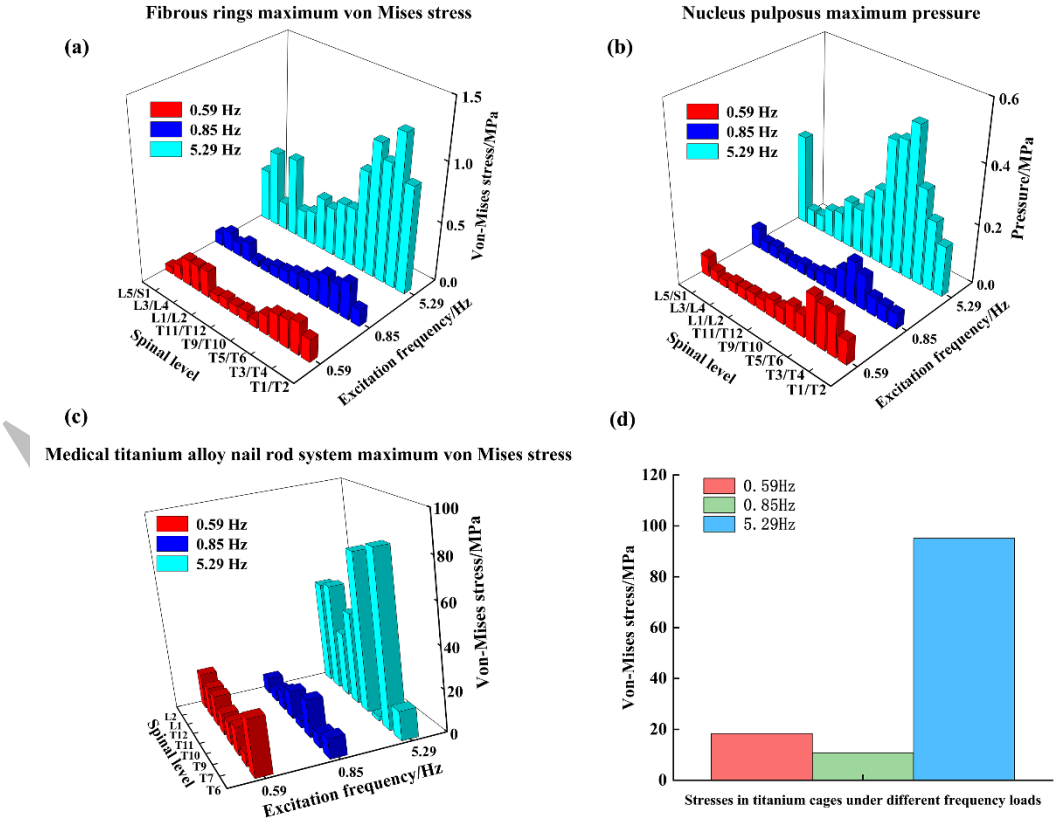

Fig. 6. Time-domain mechanical property analysis result plot (a-d).

3.3. Results of mesoscopic model bone unit analysis

The maximum stress map of the mesoscopic bone unit and the results of the structural

dynamic response of the bone unit after the removal of the stress concentration points are depicted in Fig. 7. The highest stresses are observed on the left cortical bone units X3 and S3 at the upper end face of T7 and the lower end face of T9. The macroscopic vibration mode of the model corresponds to the first-order intrinsic frequency vibration, which involves oscillation around the thoracolumbar vertebral segments along the X-axis, aligning with the actual vibration situation. Notably, the inner side of the bone plate and the bonding line experience greater stresses, and the pressure on the bone plate medium is relatively smaller. The results of the time-domain analysis of the bone unit indicate that the structural stress of each part of the bone unit exhibits the same periodic changes with the macro model cycle vibration. Compared with the anterior bone units X1 and S1 and the posterior bone units X2 and S2, the left and right bone units endure greater stress. Consequently, in a postoperative whole-body vibration environment, the cortical bone at the fusion surface of the titanium cage is more prone to stress concentrations at the corresponding locations of the lower-order vibration pattern, potentially leading to further damage. The microstrain of the bone plate was calculated based on its average stress, and then these results were converted to the displacement load applied to the microscopic model. The average stress of the bone plate, as well as the value of a in the conversion to the displacement load of the microscopic bone cells, are presented in Table 4.

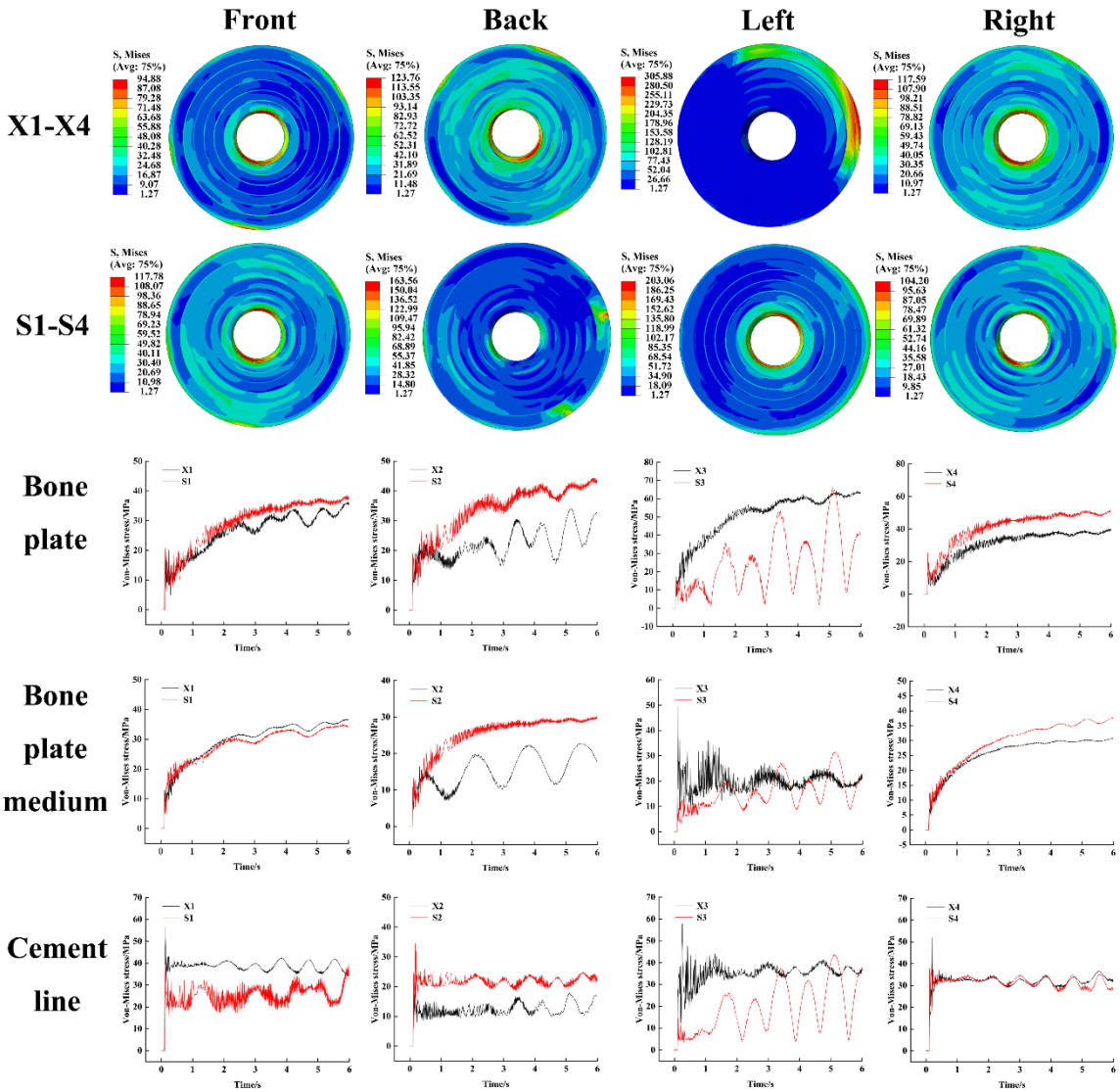

Fig. 7. Plot of the results of the kinetic analysis of the mesoscopic bone unit.

Table 4. Average stresses in the bone plate and the value of *a* in the microscopic osteoclast displacement load equation.

Bone unit numbering	**X1**	**X2**	**X3**	**X4**	**S1**	**S2**	**S3**	**S4**
Bone plate mean stress(MPa)	26.49	22.17	31.33	51.10	29.62	33.84	41.39	24.62
a value(μm)	0.0123	0.0103	0.0146	0.0238	0.0138	0.0157	0.0193	0.0115

3.4. Results of microscopic model osteoblast analysis

The maximum pore pressure and maximum pore flow velocity of the microscopic osteocytes are illustrated in the cloud diagram and statistical graph in Fig. 8. The maximum pore pressure and pore flow velocity were observed at X4 and S4 on the lower face of T7, measuring 1800 Pa and 3.21×10^{-7}m/s, respectively. The osteocytes at X3 and S3 exhibited significant pore pressure and pore flow velocity, with values of 1090 Pa and 1.95×10^{-7}m/s and 1460 Pa and 2.61×10^{-7} m/s, respectively. Notably, the maximum pore pressure of the osteocyte was located distal to the synapse, while the maximum pore flow velocity was found at the synapse near the cytosol. These microscopic findings are further corroborated by the observation that the left and right cancellous bones, affected by the first-order modal oscillations in the whole-body vibration environment, are more prone to damage.

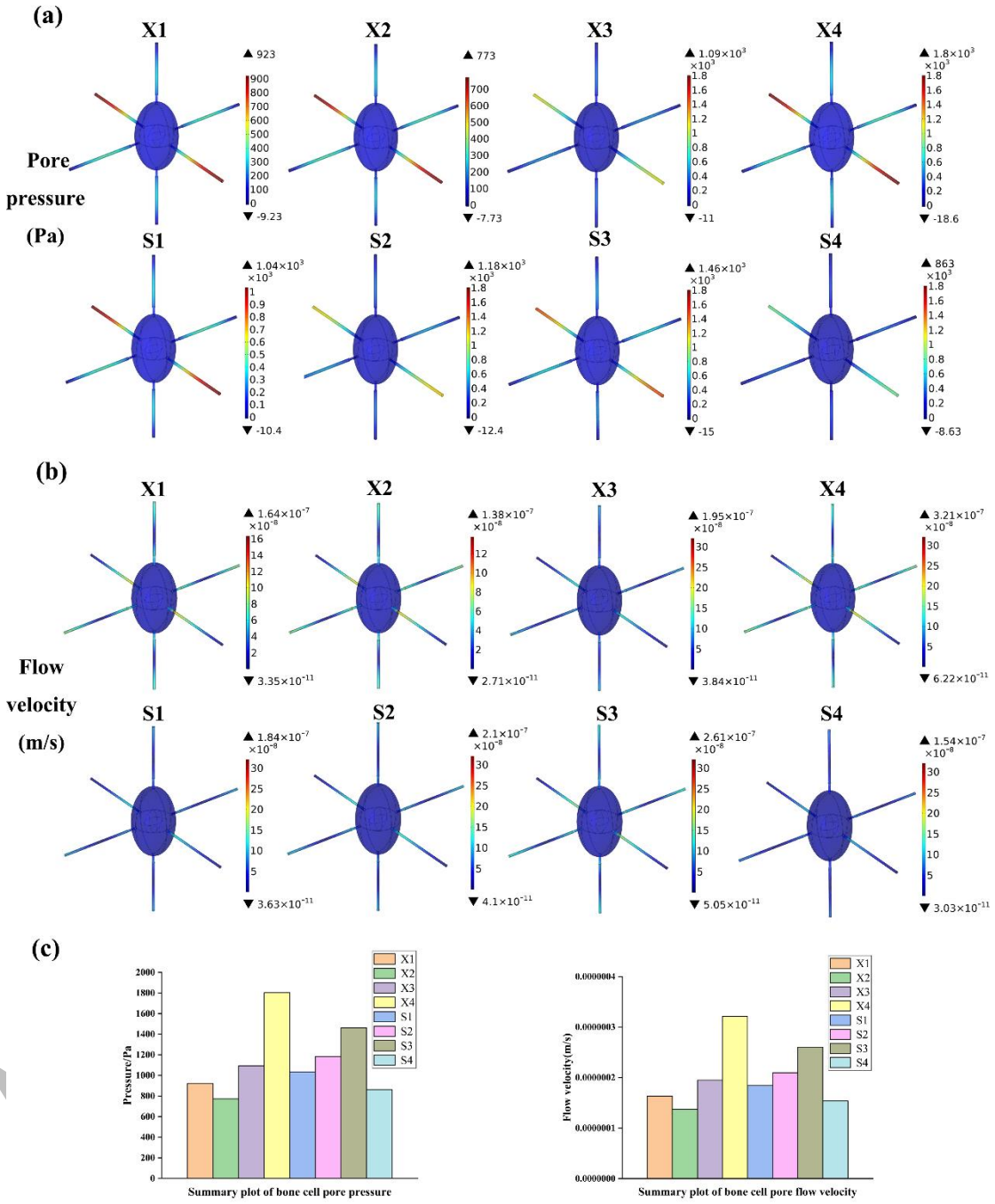

Fig. 8. Maximum pore pressure and maximum pore flow rate in bone cells.

3.5. Results of fatigue damage prediction in cancellous bone

Repeated loading below the static structural strength can impact the development of fatigue damage. The study focused on the fusion surfaces of the cancellous bone at the lower end of T7 and the upper end of T9, which were in direct contact with the titanium cage after the surgery, as well as the vertebrae of T6-L2 that were fused with the threads of the pedicle screws. Haddock et al. [11] carried out cyclic compression loading experiments on human cancellous bone trabeculae to observe their apparent fatigue behavior. They found a classical

power function relationship between the ratio of stress to elastic modulus of cancellous bone σ / E_0 and the number of cycles to failure N_f, which more accurately describes the fatigue damage behavior of cancellous bone with varying volume fractions, structures, and material properties.

$$N_f = 4.57\times10^{-18}\times\left(\sigma / E_0\right)^{-8.54}$$

According to the simulation results, the average stress in the cancellous bone at the lower end face of T7 was σ=0.09 MPa, and at the upper end face of T9, it was σ=0.23 MPa under the load of 0.59 Hz. The maximum average stress in the threaded fusion surface of the pedicle nail at L2 was σ= 0.04MPa, which was calculated by the aforementioned equation to obtain the N_f values of 4.68×10^{8}, 1.55×10^{5}, and 4.77×10^{11} times.

The average stress in the cancellous bone at the lower end face of T7 was σ=0.02MPa, and at the upper end face T9, it was σ=0.22 MPa. The maximum average stress in the threaded fusion surface of the pedicle nail at T10 was σ= 0.03 MPa under a load of 0.85 Hz, which was calculated by the aforementioned equation to obtain N_f values of 1.77×10^{14}, 2.27×10^{5}, and 5.56×10^{12} times.

Under the load of 5.29 Hz, the average stress of the cancellous bone at the lower end face of T7 was σ=0.94MPa, and at the upper end face of T9, it was σ=1.07MPa. The maximum average stress at the fusion surface of the threaded pedicle nail was σ= 0.08 MPa at L2, which was calculated using the previously mentioned equation, yielding N_f values of 1.72×10^{2}, 2.67×10^{3}, and 1.28×10^{9} times. It can be concluded that medical implants are unlikely to cause fatigue damage to the cancellous bone of the fusion surface under low load vibrations; however, the fatigue life of cancellous bone will be significantly reduced under high load vibrations.

4. Discussion

This study offers a novel perspective for analyzing the vibration response and fatigue damage in patients with severe lateral kyphosis of the spine, who are exposed to whole-body vibration after orthopedic surgery. The modal, time-domain, and frequency-domain responses of the spine were initially investigated on a macroscopic scale, revealing that the first three intrinsic frequency vibration modes, especially the first intrinsic frequency vibration mode, exert the greatest influence on the macroscopic model. The mesoscopic model of the bone unit located near the fusion surface of the titanium cage was established using the sub-modeling technique, and stress changes of the bone unit under whole-body vibration were examined. Subsequently, the microstresses of the mesoscopic bone unit were converted into

microstrains loaded onto the microscopic model of bone cells, and the pore pressure and pore flow velocity of the bone cells were assessed. At last, based on the classical fatigue damage prediction formula, the number of fatigue damage cycles of titanium cage fusion surfaces and pedicle nail fusion surfaces under the first three orders of intrinsic frequency excitation were predicted.

For the macroscopic model, the first-order intrinsic frequency of the patient was determined through modal analysis to be (0.59 Hz) higher than the T1-S1 first-order resonance frequency (0.41 Hz) reported in the standard human spine model of Kong et al. [13]. This discrepancy may be attributed to the addition of medical implants from the patient's orthopaedic surgery, which increased the stiffness of the spine. Frequency domain analysis identified the first three orders of intrinsic frequency as the main resonance region of the spine, particularly around the first and second-order intrinsic frequencies, where the patient's spine exhibited significant displacement response. This observation is consistent with the fact that the lower-order modes of vibrational mechanics involve a greater effective mass, have the highest energy, and exert the most substantial impact. The amplitudes of the first two modes are particularly noteworthy, likely due to medical implants restricting the mobility of the vibration mode corresponding to the third-order mode. The frequency domain results indicated that the maximum displacement occurred in the L3 segment, contrasting with the findings by Li et al. [17], which reported that the maximum displacement occurred in the thoracic spine segment. This difference may stem from the selected segments being located at the upper and lower ends of the titanium cage, with the implantation of the titanium cage reducing the mobility of the joints and consequently concentrating the vibration displacements primarily in the lumbar spine segments. The results of time-domain analysis demonstrated that under the first-order intrinsic frequency excitation, the displacement in the X-direction exhibited a significant amplification trend, while the displacement in the Y-direction also gradually increased. The first-order resonance is more likely to induce secondary damage to the patient, and exposure to the vibration environment of the first-order intrinsic frequency should be avoided. Under the second-order intrinsic frequency excitation, the Y-direction displacement also displayed a slow amplification trend, suggesting that the second-order intrinsic frequency excitation may harm the spine. Under the third-order intrinsic frequency excitation, the displacements in all three directions increased gradually. This may be because the implantation of pedicle pins and titanium cages in the patient's spine after orthopedic surgery significantly limited the mobility of the spine model in the Z-axis direction and caused the vibration response to increase slowly. For the mesoscopic model, the

maximum stress in the bone unit was borne by the bone plate. However, in contrast to the hydrostatic study by Yu et al. [35], the maximum stress occurred in the innermost bone plate, indicating that the inner Havers tube will experience greater stress in the vibration environment. Compared to the hydrostatic study of the mesoscopic bone unit, stresses are generally magnified several times under vibration conditions, supporting the conclusion that dynamic cyclic loading is more likely to cause damage to the structure. Elevated stresses are beneficial in stimulating tissue fluid flow in the region, thereby promoting cellular regeneration (Ganesh et al. [9]), while lower stresses on bonding wires and bone plate media are beneficial for self-protection of the bone structure.

For the microscopic model, the increased pore pressure and pore flow velocity of the cell synapse facilitate fluid movement, thereby enhancing osteocyte metabolism and information exchange and guiding osteoblasts to carry out bone reconstruction [25], [26]. Osteoblasts located in areas corresponding to the vibration pattern have greater pore pressure and pore flow velocity, indicating that the use of effective vibration can better stimulate osteoblast growth, thus accelerating the building of new mesoscopic bone units. This, in turn, has a positive impact on macroscopic bone growth, benefiting patients recovering from surgery.

Repeated loading of cancellous bone below static structural strength leads to fatigue damage, with bone trabeculae being the primary contributors to the damage behavior of the vertebral body. According to the fatigue damage prediction results of cancellous bone in this study, under low load vibration conditions, fatigue damage to the cancellous bone of pedicle pins, as well as titanium cage fusion surfaces, is generally minimal. However, the fatigue life of cancellous bone is significantly reduced under high-load vibration conditions, suggesting that heavier patients should be more careful to avoid exposure to vibrations compared to lighter patients.

This study also acknowledges several limitations: the macroscopic model did not account for the impact of the spinal cord on the spine, the mesoscopic model of the bone unit did not consider the irregular bone structure around it, the microscopic model of the LCS failed to consider the interstitial fluid in the bone canal and the bone cavity, and the fatigue injury prediction did not take the osteoporosis condition into account. Future research should incorporate additional factors when constructing macroscopic, mesoscopic, and microscopic models to enhance their realism. It is noteworthy that investigating the effects of vibration environment on stimulating bone growth will further advance our understanding of the growth mechanism of human bone tissue.

5. Conclusion

Spinal orthopedic implants, such as titanium cages and pedicle screws, change the mobility of the adjacent segments and produce a stress shielding effect that impacts the fusion of the bone tissues. Meanwhile, mesoscopic bone cells experience greater stresses under vibration compared to static loads, with peak stresses occurring at locations consistent with modal vibration. In addition, microscopic bone cell synapses exhibit higher pore pressures and pore flow velocities under vibration than under static loads, facilitating cell growth. Moreover, low load vibration generally does not induce fatigue damage to the cancellous bone at the fusion surface of medical implants.

Acknowledgments

The authors would like to express their gratitude to all reviewers who participated in the review.

Funding

This work is supported by grants from National Natural Science Foundation of China (Grant No. 32260235).

Author contributions

Yuxuan Zhang: Preparation of the manuscript; he execution of research. Rongchang Fu: Obtain financing; The preparation of the research program. Pengju Li: Guidance on technology.

Conflict of interest

The authors declare that they have no conflict of interest.

References

[1] Basso N., Heersche J.N.M., Characteristics of in vitro osteoblastic cell loading models, Bone, 2002, 30(2), 347–351, DOI:10.1016/S8756-3282(01)00678-0.

[2] Chen C.S., Cheng C.K., Liu C.L., Lo W.H., Stress analysis of the disc adjacent to interbody fusion in lumbar spine, Med Eng Phys, 2001, 23(7), 485–493, DOI:10.1016/s1350-4533(01)00076-5.

[3] Chen J., Xu T., Zhou J., Han B., Wu Q., Jin W., Zhang X., The superiority of Schroth exercise combined brace treatment for mild-to-moderate adolescent idiopathic scoliosis: A systematic review and network meta-analysis, World Neurosurg, 2024, 186, 184–196.e9, DOI:10.1016/j.wneu.2024.03.103.

[4] Chen K.J., The conduction of poroelastic mechanical signals from osteon to osteocyte scale, Master thesis, Taiyuan University of Technology, 2019. (in Chinese)

[5] Danielsson A.J., Natural history of adolescent idiopathic scoliosis: a tool for guidance in

decision of surgery of curves above 50°, J Child Orthop, 2013, 7(1), 37–41, DOI:10.1007/s11832-012-0462-7.

[6] Duncan R.L., Turner C.H., Mechanotransduction and the functional response of bone to mechanical strain, Calcif Tissue Int, 1995, 57(5), 344–358, DOI:10.1007/BF00302070.

[7] Erbulut D.U., Zafarparandeh I., Lazoglu I., Ozer A.F., Application of an asymmetric finite element model of the C2-T1 cervical spine for evaluating the role of soft tissues in stability, Med Eng Phys, 2014, 36(7), 915–921, DOI:10.1016/j.medengphy.2014.02.020.

[8] Fang X., Zhao G., Wang C., Bai L., Yan W., Ma T., Establishment and analysis of finite element model of lumbar spine L4~L5 segment based on CT images, Chin J Biomed Eng, 2014, 31(4), 487–492, DOI:10.3969/j.issn.0258-8021.2014.04.014. (in Chinese)

[9] Ganesh T., Laughrey L.E., Niroobakhsh M., Lara-Castillo N., Multiscale finite element modeling of mechanical strains and fluid flow in osteocyte lacunocanalicular system, Bone, 2020, 137, 115328, DOI: 10.1016/j.bone.2020.115328.

[10] Ghanbari J., Naghdabadi R., Nonlinear hierarchical multiscale modeling of cortical bone considering its nanoscale microstructure, J Biomech, 2009, 42(10), 1560–1565, DOI:10.1016/j.jbiomech.2009.02.014.

[11] Haddock S.M., Yeh O.C., Mummaneni P.V., Rosenberg W.S., Keaveny T.M., Similarity in the fatigue behavior of trabecular bone across site and species, J Biomech, 2004, 37(2), 181–187, DOI:10.1016/S0021-9290(03)00245-8.

[12] Koller H, Koller J, Mayer M, Hempfing A, Hitzl W., Osteotomies in ankylosing spondylitis: where, how many, and how much, Eur Spine J, 2018, 27(Suppl 1), 70–100, DOI:10.1007/s00586-017-5421-z.

[13] Kong W.Z., Goel V.K., Ability of the finite element models to predict response of the human spine to sinusoidal vertical vibration, Spine, 2003, 28(17), 1961–1967, DOI:10.1097/01.BRS.0000083236.33361.C5.

[14] Lafage V., Schwab F., Patel A., Hawkinson N., Farcy J.P., Pelvic tilt and truncal inclination: two key radiographic parameters in the setting of adults with spinal deformity. Spine, 2009, 34(17), E599, DOI:10.1097/BRS.0b013e3181aad219.

[15] Le P., Solomonow M., Zhou B.H., Lu Y., Patel V., Cyclic Load Magnitude is a Risk Factor for a Cumulative Lower Back Disorder, J Occup Environ Med, 2007, 49(4), 375–387, DOI:10.1097/JOM.0b013e318046eb0b.

[16] Li P., Fu R., Yang X., Wang K., Chen H., Finite Element Method-Based Study for Spinal Vibration Characteristics of the Scoliosis and Kyphosis Lumbar Spine to Whole-Body Vibration Under a Compressive Follower Preload, Comput Methods Biomech Biomed

Engin, 2024, 1–10, DOI: 10.1080/10255842.2024.2333925.
[17] Li P., Fu R., Yang X., Wang K., Dynamic Response of Idiopathic Scoliosis and Kyphosis Spine, J Shanghai Jiaotong Uni (Sci), 2025, 30(3), 478–487, DOI:10.1007/s12204-023-2635-6.
[18] Li X.F., Liu Z.D., Dai L.Y., Zhong G.B., Zang W.P., Dynamic response of the idiopathic scoliotic spine to axial cyclic loads, Spine, 2011, 36(7), 521–528, DOI:10.1097/BRS.0b013e3181d55fb0.
[19] Lievers W.B., Poljsak A.S., Waldman S.D., Pilkey A.K., Effects of dehydration-induced structural and material changes on the apparent modulus of cancellous bone, Med Eng Phys, 2010, 32(8), 921–925, DOI: 10.1016/j.medengphy.2010.06.001.
[20] Liu Q., Zhang Q., Zhang C.Q., Wang A.G., Xu Z.C., Song S.X., Jia T.J., Li K., The effect of failure mechanics on the fatigue responses of lumbar intervertebral disc, J Biomech, 2024, 176, 112363, DOI:10.1016/j.jbiomech.2024.112363.
[21] Markolf K.L., Morris J.M., The structural components of the intervertebral disc. A study of their contributions to the ability of the disc to withstand compressive forces, J Bone Joint Surg Am, 1974, 56(4), 675–687, DOI:10.1111/j.1748-1716.1957.tb01378.x.
[22] Momeni Shahraki N., Fatemi A., Goel V.K., Agarwal A., On the Use of Biaxial Properties in Modeling Annulus as a Holzapfel–Gasser–Ogden Material, Front Bioeng Biotechnol, 2015, 3, 69, DOI:10.3389/fbioe.2015.00069.
[23] Nachemson A.L., Schultz A.B., Berkson M.H., Mechanical properties of human lumbar spine motion segments. Influence of age, sex, disc level, and degeneration, Spine, 1979, 4(1), 1–8, DOI:10.1097/00007632-197901000-00001.
[24] Panjabi M.M., Krag M.H., White A.A. 3rd, Southwick W.O., Effects of preload on load displacement curves of the lumbar spine, Orthop Clin North Am, 1977, 8(1), 181192, DOI:10.1016/S0030-5898(20)30944-5.
[25] Piekarski K, Munro M., Transport mechanism operating between blood supply and osteocytes in long bones, Nature, 1977, 269(5623), 80–82, DOI:10.1038/269080a0.
[26] Smit T.H., Huyghe J.M., Cowin S.C., Estimation of the poroelastic parameters of cortical bone, J Biomech, 2002, 35(6), 829–835, DOI:10.1016/S0021-9290(02)00021-0.
[27] Tian, H., Shi, X.K., Distribution of body mass in young men in China, Journal of Jilin Medical College, 2001. (in Chinese)
[28] Wang C., Hu W., Li J., Hu F., Wang T., Zhang H., Wang Y., Hao Y., Zhang X., Wang Y., Progress in the study of commonly used posterior osteotomy styles for the treatment of spinal deformity, J Spine Surg, 2018, 16(6), 368–374+383,

DOI:CNKI:SUN:JZWK.0.2018-06-012. (in Chinese)
[29] Wang L., Dong J., Xian C.J., Computational Investigation on the Biomechanical Responses of the Osteocytes to the Compressive Stimulus: A Poroelastic Model, Biomed Res Int, 2018, 2018, 4071356, DOI:10.1155/2018/4071356.
[30] Wang Y., Dong H., Yan Y., Yu J., Wu X., Wang Y., Xue Y., Wang X., Wei X., Li P., Chen W., Biomechanical analysis of a lacunar-canalicular system under different cyclic displacement loading, Comput Methods Biomech Biomed Engin, 2023, 26(15), 1806–1821, DOI:10.1080/10255842.2022.2145889.
[31] Wang Z., Fu R., Ma Y., Ye P., [Macroscopic and mesoscopic biomechanical analysis of the bone unit in idiopathic scoliosis], J Biomed. Eng, 2023, 40(2), 303–312, DOI: 10.7507/1001-5515.202212053.
[32] Weinstein S.L., Zavala D.C., Ponseti I.V., Idiopathic scoliosis: long-term follow-up and prognosis in untreated patients, J Bone Joint Surg Am, 1981, 63(5), 702, DOI:10.2106/00004623-198163050-00003.
[33] Yamamoto I., Panjabi M.M., Crisco T., Oxland T., Three-dimensional movements of the whole lumbar spine, Spine (Phila Pa 1976), 1989, 14(11), 1256–1260, DOI:10.1016/0021-9290(89)90523-X.
[34] Yan W., Zhao G., Fang X., Guo H., Ma T., Tu Y., Finite element modeling and analysis of human lumbar spine L4-5 segments, J Biomed Eng, 2014, 31(3), 612–618, DOI:CNKI:SUN:SWGC.0.2014-03-028. (in Chinese)
[35] Yu W.L., Study on the Multi-scale Conduction Behavior of Fluid Stimulation in Loaded Bone, PhD thesis, Taiyuan University of Technology, 2020. (in Chinese)
[36] Zahaf S., Kebdani S., Ghalem M., Mestar A., Zina N., Aour B., Biomechanical evaluation of two posterior lumbar intervertebral fusion surgical scenarios reinforced by a rigid posterior fixation system in the vertebral column analyzed by the finite element method, Nano Biomed Eng, 2018, 10(3), 258–278, DOI: 10.5101/nbe.v10i3.p258-278.
[37] Zahaf S., Mansouri B., Belarbi A, Azari Z., The Effect of the Posterior Loading on the Spine of a School Child, Adv Cancer Prev, 2016, 1(3), 1000112, DOI:10.4172/2472-0429.1000112.
[38] Zheng J., Weng L.Q., Shi M.Y., Zhou J., Hua L.C., Qian L.M., Zhou Z.R., Effect of water content on the nanomechanical properties and microtribological behaviour of human tooth enamel, Wear, 2013, 301(1–2), 316–323, DOI:10.1016/j.wear.2012.12.043

566